





A computational description of time-dependent transport of a water-based nanofluid with hybrid nanocomposite Cu–Al₂O₃ over a parabolic surface by Keller-box scheme: A modified Buongiorno model

Sohita Rajput ^{*}, Krishnendu Bhattacharyya ^{*,‡}, Dimpal Sharma ^{*},
Amit Kumar Pandey^{*} and Ali J. Chamkha [†]

^{*}*Department of Mathematics, Institute of Science,
Banaras Hindu University, Varanasi 221005,
Uttar Pradesh, India*

[†]*Faculty of Engineering,
Kuwait College of Science & Technology,
7th Ring Road, Doha Area, Kuwait*

[‡]*krishnendu.math@gmail.com; krishmath@bhu.ac.in; krish.math@yahoo.com*

Received 28 March 2023

Revised 24 July 2023

Accepted 19 August 2023

Published 23 November 2023

This paper discusses the high heat transfer demand from application prospects. Hybrid nanofluid is a well-known liquid with higher heat transfer capabilities. Here, the time-dependent flow of hybrid nanocomposite, by hybridizing the metal (Cu) and metallic oxide (Al₂O₃) and inserting them into water-based nanofluid, is examined. The flow takes place over the upper half of a parabolic surface. The modified Buongiorno model is used to express the physical phenomenon in mathematical equations form. The governing system of partial differential equations (PDEs) is reduced to a system of ordinary differential equations (ODEs) by applying certain transformations. Computation of the final equations has been done by a numerical scheme, known as the Keller-box method. The significance of dimensionless flow causing physical parameters is shown through graphs and tables. The findings reveal that among the hybrid nanofluids with two types of nanoparticles varying from 0% to 5%, a nanofluid having 5% of both nanoparticles is the one with the maximum surface drag force and heat transport rate, which are 41.8% and 22.7% higher to water, respectively. A higher amount of Al₂O₃ than Cu results in a suitable hybrid combination for application purposes to produce higher cooling rate with less surface drag. Also, the thickness of the surface, unsteadiness, nanoparticles suspension and power index of wall temperature enhance the heat transfer rate. Thin parabolic surfaces experience less drag and have larger boundary layer thicknesses (momentum, thermal and concentration) as compared to thicker parabolic surfaces. Also, the addition of copper slows down the hybrid fluid flow field, but alumina magnifies the mobility of hybrid fluid.

Keywords: Water-based nanofluid; Cu–Al₂O₃ hybrid nanocomposite; modified Buongiorno model; parabolic surface; unsteady flow; Keller-box method.

[‡]Corresponding author.

Nomenclature

- A : Unsteadiness parameter
 b : Constant
 B : Constant
 C : Concentration of nanoparticles
 C_{fr} : Local skin friction coefficient
 C_w : Concentration at the wall
 C_∞ : Concentration in free-stream
 D_B : Brownian diffusion coefficients ($m^2 \cdot s^{-1}$)
 D_T : Thermophoretic diffusion coefficients ($m^2 \cdot s^{-1}$)
 f : Dimensionless stream function
 F : Dimensionless stream function
 m : Velocity power index
 n : Temperature/concentration power index
 Nb : Brownian motion parameter
 Nt : Thermophoresis parameter
 Nu_x : Local Nusselt number
 Pr : Prandtl number
 q_m : Wall mass flux ($m \cdot s^{-1}$)
 q_w : Wall heat flux ($W \cdot m^{-2}$)
 Re_x : Local Reynolds number
 Sc : Schmidt number
 Sh_x : Local Sherwood number
 t : Time (s)
 T : Temperature of nanofluid (K)
 T_w : Temperature at the wall (K)
 T_∞ : Temperature in free-stream (K)
 u, v : Velocity components in the x - and y -directions, respectively ($m \cdot s^{-1}$)
 u_w : Velocity at the wall ($m \cdot s^{-1}$)
 U_0 : Constant
 x, y : Cartesian coordinate system (m)

Greek Symbols

- α : Constant (s^{-1})
 ζ : Variable
 η : Variable
 Θ : Dimensionless temperature
 θ : Dimensionless temperature

- κ : Thermal conductivity ($\text{Wm}^{-1} \cdot \text{K}^{-1}$)
- μ : Viscosity ($\text{kg} \cdot \text{m}^{-1} \cdot \text{s}^{-1}$)
- ρ : Density ($\text{kg} \cdot \text{m}^{-3}$)
- (ρc_p) : Heat capacity ($\text{JK}^{-1} \cdot \text{m}^{-3}$)
- τ : Ratio of heat capacities
- τ_w : Wall shear stress ($\text{Wm}^{-1} \cdot \text{s}^{-2}$)
- ν : Kinematic viscosity ($\text{m}^2 \cdot \text{s}^{-1}$)
- Φ : Dimensionless concentration
- ϕ : Dimensionless concentration
- χ : Wall thickness parameter
- ψ : Stream function

Subscripts

- 1, 2 : Properties for Cu and Al_2O_3 , respectively
- w : Boundary condition at the wall
- f : Base fluid
- nf : Cu nanofluid
- hnf : Hybrid nanofluid
- ∞ : Boundary condition in free-stream

1. Introduction

In the present era of technology, improvement in heat transfer performance of the systems has become a common issue. Conventionally, solid particles (metal, metal oxides, metal nitrates, carbide ceramics, semiconductors and carbon in various forms) have more thermal conductivity than the traditional fluids (water, ethylene glycol, transformer oil and polymer solutions). So, the idea is that the dispersion of these particles into base fluids may significantly enhance the heat transfer rate. Nano-sized solid particles have been preferred as suspended items over the macro- and micro-sized ones to get a stable suspension with less settling effect due to gravity since these particles are roughly equivalent in size to the base fluid molecules. Thus, liquids with dispersed nanoparticles are used in many applications (heat exchangers, cooling systems, solar collectors, sensing outlets, energy conversion, etc.¹⁻⁴) as a heat transfer medium to improve the final quality of a product. This novel concept was proposed by Choi.⁵ Eastman *et al.*⁶ noticed that dispersion of Cu nanoparticles of size less than 10 nm into the base fluid ethylene glycol enhances the thermal conductivity of the resulting nanofluid by 40%. Further, a study of nanofluid to analyze the enhancement in heat transport characteristics, by mixing $\gamma\text{-Al}_2\text{O}_3$ into deionized water, was performed by Wen and Ding.⁷ Shafiq *et al.*⁸ considered the bioconvective flow of nanofluid with zero mass flux boundary constraint; also, the Darcy–Forchheimer flow of carbon nanotubes toward a rotating disk was discussed by these

authors.⁹ A comprehensive investigation on the heat transmission characteristics of Sutterby nanofluid flow was carried out by Gowda *et al.*¹⁰ with energy diffusion using the Cattaneo–Christov model and Stefan blowing condition. Their study revealed that Stefan blowing is the responsible factor for augmenting both the tangential and radial velocity gradients. Recently, to know the uses of nanofluids in various fields with different flow scenarios, theoretical investigations have been conducted by many researchers.^{11–21}

There are some issues faced by nanofluids such as attaining long-term stability and having a low-cost suspension. These challenges may be resolved to a certain level by using different types of nanoparticles or nanocomposites based on the trade-off between the advantages and disadvantages of the individual particles. For example, Cu is chemically reactive and unstable, and possesses high thermal conductivity, while Al₂O₃ possesses lower thermal conductivity but exhibits good stability and chemical inertness. By hybridizing these nanoparticles, the resulting fluid possesses better thermo-physical properties with modified heat transfer characteristics. These types of nanofluids are known as hybrid nanofluids and are used to get the synergistic effect of the suspended particles. The efficiency of hybrid nanofluid is attributed to the nanoparticles' synergistic effect, good aspect ratio and better thermal work. In the literature, hybrid nanofluid is found to be more thermally and economically beneficial than mono-nanofluid. In a review article by Babu *et al.*, the synthesis, preparation and application of various hybrid nanofluids were discussed.²² The improvement in the thermal transport mechanism (convection) of water-driven hybrid nanofluid Cu–Al₂O₃ was analyzed by Suresh *et al.*²³ Devi and Devi²⁴ performed a comparative study between Cu–Al₂O₃/water and Cu/water for heat transport performance. They found a significant improvement in the rate of heat transfer of Cu–Al₂O₃/water than Cu/water. Further, in another study,²⁵ they disclosed a 11.2% enhancement in the heat transport rate of Cu–Al₂O₃/water as compared to Cu/water, whereas a 17.3% enhancement than the traditional fluid, water. A study of Casson hybrid nanofluid flow over a Riga plate with thermophoretic mass diffusion was conducted by Madhukesh *et al.*²⁶ in the presence of a porous medium, and they concluded that the velocity of working fluid declines with porosity parameter. Recently, many researchers^{27–30} have explained the flow of different hybrid nanofluids with several physical aspects.

In the literature, there are two mathematical models which are frequently used by researchers, namely single- and two-phase models, to analyze the nanofluid flow characteristics. Single-phase model is also known as the homogeneous model because in this model the volume fraction of the nanoparticles remains constant at every point of the fluid. This homogenous model was proposed by Tiwari and Das.³¹ On the other hand, a two-phase model was proposed by Buongiorno³²; this model considers the slip mechanisms between nanoparticles and traditional fluid, but ignores the thermo-physical properties of the nanoparticles. Time-dependent flows of nanofluid modeled by Buongiorno considerations were analyzed by Ali *et al.*^{33,34} Many researchers are continuously working to develop it as an advanced two-phase model

so that it can describe the transportation of nanofluids efficiently, for two-phase nanofluid flows. Lately, this model was refined by Yang *et al.*³⁵ to take care of nanoparticles' thermo-physical properties in momentum and energy equations, known as the modified Buongiorno model (MBM). The purpose of combining two types of nanofluid models is to take into consideration the multiple mechanisms affecting nanofluid behavior and to improve the accuracy and applicability of the overall nanofluid modeling technique. Each model has strengths and limitations, and by combining them, researchers hope to take the maximum advantages of each to provide a more thorough and realistic picture of nanofluid behavior. A modified model enhances the ability to predict and understand heat transfer and fluid flow in nanofluids across a wide range of applications, including thermal management, energy systems and advanced cooling technologies. Sheikholeslami *et al.*³⁶ studied the free convection MHD flow of Al_2O_3 /water considering MBM, while the mixed convection flow of Al_2O_3 /water was analyzed by Malvandi and Ganji³⁷ in micro-channels. MBM was utilized by Siddheshwar and Lakshmi³⁸ to investigate the heat transfer of nanofluids in cylindrical enclosures and cylindrical annuli. Comprehensive discussions on MBM were made by researchers^{39–43} to study the heat transport mechanisms of nanofluids.

The occurrence of multitudinous flow over a surface with variable thickness can be observed in many fields, such as aviation, space science and many industries. Geometrically, the paraboloid of revolution is described as the upper-half face of a body with variable thickness. Some examples of flow over a paraboloid surface include the flow past the pointed edge of an aircraft, rocket, bullet and bonnet of a car. Flow over the slender surfaces was studied by Lee⁴⁴ in 1967. Later, Davis and Werle⁴⁵ investigated the flow behavior past a paraboloid object numerically. Due to the vast applications of nanofluids, many researchers contributed to investigating the heat transport performance of the nanofluid over the paraboloid of revolution. Bioconvection in MHD nanofluid flow over the upper-half surface of flow geometry with variable thickness was studied by Makinde and Animasaun^{46,47} with the consideration of nonlinear thermal radiation. Animasaun⁴⁸ and Animasaun and Sandeep⁴⁹ devised the flow of water-driven Al_2O_3 with 47-nm and 36-nm Al_2O_3 /water, respectively. More works on the parabolic surface were carried out by Fang *et al.*,⁵⁰ Khan *et al.*,⁵¹ Olabode *et al.*⁵² and Reddy and Reddy.⁵³ Whereas, artificial neural network (ANN)-based studies of nanofluid flow past a needle were conducted by Shafiq *et al.*⁵⁴ with ethylene glycol-based nanofluid with single-walled carbon nanotubes concerning the aspects of nanoparticles' diameter and solid–fluid interfacial layer; also, the Soret and Dufour effects were considered by them in another work.⁵⁵ Nayak *et al.*⁵⁶ performed a comparative analysis of various metallic and metallic oxide nanoparticles for the heat transfer characteristics over a thin needle.

This computational work involves the study of water-based hybrid nanofluid with nanomaterials by hybridizing the metallic (Cu) and metallic oxide (Al_2O_3) nanoparticles. This study aims to analyze the unsteady flow governed through

a horizontally moving parabolic surface. The novelty aspects of this work are: (i) consideration of the impacts of hybridization of nanoparticles in nanofluid flow past a parabolic surface; and (ii) an extended form of the Buongiorno model is implemented to model the nanofluid flow. Some suitable variables are used to transform the constructed flow-representative partial differential equations (PDEs) into ordinary differential equations (ODEs). A very effective numerical technique known as the “Keller-box” method (KBM) is applied to find the solution to the coupled ODEs. The obtained results are validated by developing an excellent agreement with the solution found by another well-established numerical method “bvp4c”, a MATLAB solver, and early published findings in the literature. Results are analyzed against flow-involved parameters by plotting the respective profiles. We will try to emphasize on the following research questions:

- (a) How do we control surface drag force and heat transfer rate with the addition of different amounts of Cu and Al_2O_3 in hybrid nanofluid flow on the upper parabolic surface?
- (b) What are the simultaneous effects of unsteadiness and power index parameters?
- (c) How does surface thickness play a vital role in unsteady flow dynamics?

2. Formulation of the Problem

We have considered two-dimensional incompressible hybrid nanofluid flow over an upper parabolic surface. The Cartesian coordinate system is taken in such a manner that x -axis lies along the direction of fluid flow and y -axis is in the normal direction of the fluid flow. Physical model of the problem is shown in Fig. 1. The motion of the fluid is confined in the domain $B\sqrt{1 - \alpha t}(x + b)^{\frac{1-m}{2}} \leq y < \infty$.⁵³ Here, B is a constant

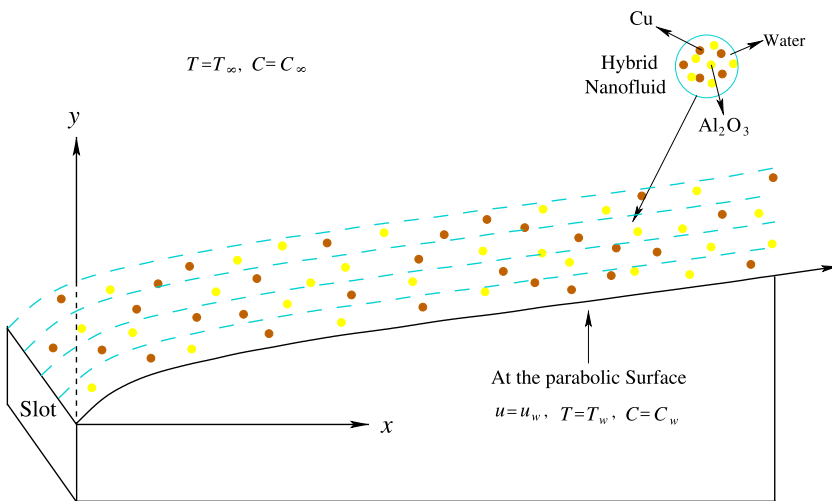


Fig. 1. (Color online) Physical sketch of the problem.

and is small, so the surface is sufficiently thin to avoid the pressure gradient along the surface. $\alpha (> 0)$ is the representative of time scale with dimension time^{-1} , b is the sheet stretching rate parameter and m is the power-law exponent (where $m < 1$ stands for the parabolic surface and $m = 1$ represents a flat plate). We have considered the following assumptions regarding the motion of fluid:

- Flow is laminar and time-dependent.
- The surface velocity of the fluid is considered as $u_w(x, t) = U_0(x + b)^m / (1 - \alpha t)$.
- Water is taken as the working fluid.
- Nonisothermal wall temperature $T_w(x, t) = T_\infty + B(x + b)^{\frac{1-m}{2}} / (1 - \alpha t)^n$ and nonisosolutal wall concentration $C_w(x, t) = C_\infty + B(x + b)^{\frac{1-m}{2}} / (1 - \alpha t)^n$ are considered, where T_∞ and C_∞ are free-stream temperature and concentration and n is the power-law index.

The modified Buongiorno model is used to mathematically express the nanofluid flow problem with the conservation of mass, momentum, energy and concentration equations. The flow-governing nonlinear and coupled boundary layer equations can be given as follows^{40,52}:

$$\frac{\partial u}{\partial x} + \frac{\partial v}{\partial y} = 0, \tag{1}$$

$$\frac{\partial u}{\partial t} + u \frac{\partial u}{\partial x} + v \frac{\partial u}{\partial y} = \nu_{\text{hnf}} \frac{\partial^2 u}{\partial y^2}, \tag{2}$$

$$\frac{\partial T}{\partial t} + u \frac{\partial T}{\partial x} + v \frac{\partial T}{\partial y} = \alpha_{\text{hnf}} \frac{\partial^2 T}{\partial y^2} + \tau \left[D_B \frac{\partial T}{\partial y} \frac{\partial C}{\partial y} + \frac{D_T}{T_\infty} \left(\frac{\partial T}{\partial y} \right)^2 \right], \tag{3}$$

$$\frac{\partial C}{\partial t} + u \frac{\partial C}{\partial x} + v \frac{\partial C}{\partial y} = D_B \frac{\partial^2 C}{\partial y^2} + \frac{D_T}{T_\infty} \frac{\partial^2 T}{\partial y^2} \tag{4}$$

subject to the boundary conditions

$$\left. \begin{aligned} t < 0 : u = 0, \quad v = 0, \quad T = T_\infty, \quad C = C_\infty & \quad \text{for any } x, y, \\ t \geq 0 : u = u_w(x, t), \quad v = 0, \quad T = T_w, \quad C = C_w & \quad \text{for } y = B\sqrt{1 - \alpha t}(x + b)^{\frac{1-m}{2}}, \\ u \rightarrow 0, \quad T \rightarrow T_\infty, \quad C \rightarrow C_\infty & \quad \text{for } y \rightarrow \infty, \end{aligned} \right\} \tag{5}$$

where u and v are the components of velocity along the x - and y -axes, respectively, T is the temperature of the nanofluid, C is the concentration of nanoparticles, $\nu_{\text{hnf}} = \mu_{\text{hnf}} / \rho_{\text{hnf}}$ is the kinematic viscosity of hybrid nanofluid, D_B and D_T are Brownian and thermophoretic diffusion coefficients, $\alpha_{\text{hnf}} = \kappa_{\text{hnf}} / (\rho c_p)_{\text{hnf}}$ is the thermal diffusivity of hybrid nanofluid and τ is the ratio of heat capacity of nanoparticles to the heat capacity of fluid. μ_{hnf} , ρ_{hnf} , κ_{hnf} and $(\rho c_p)_{\text{hnf}}$ are the viscosity, density, thermal conductivity and heat capacity of hybrid nanofluid, respectively, which are defined

as follows³⁰:

$$\left. \begin{aligned} \rho_{\text{hnf}} &= [(1 - \phi_2)\{(1 - \phi_1)\rho_f + \phi_1\rho_1\} + \phi_2\rho_2], & \frac{\mu_{\text{hnf}}}{\mu_f} &= \frac{1}{(1 - \phi_1)^{2.5}(1 - \phi_2)^{2.5}}, \\ (\rho c_p)_{\text{hnf}} &= [(1 - \phi_2)\{(1 - \phi_1)(\rho c_p)_f + \phi_1(\rho c_p)_1\} + \phi_2(\rho c_p)_2], \\ \frac{\kappa_{\text{hnf}}}{\kappa_f} &= \frac{\kappa_{\text{hnf}}}{\kappa_{\text{nf}}} \times \frac{\kappa_{\text{nf}}}{\kappa_f}, & \frac{\kappa_{\text{hnf}}}{\kappa_{\text{nf}}} &= \frac{\kappa_2 + 2\kappa_{\text{nf}} - 2\phi_2(\kappa_{\text{nf}} - \kappa_2)}{\kappa_2 + 2\kappa_{\text{nf}} + \phi_2(\kappa_{\text{nf}} - \kappa_2)}, \\ \frac{\kappa_{\text{nf}}}{\kappa_f} &= \frac{\kappa_1 + 2\kappa_f - 2\phi_1(\kappa_f - \kappa_1)}{\kappa_1 + 2\kappa_f + \phi_1(\kappa_f - \kappa_1)}, \end{aligned} \right\} \quad (6)$$

where ϕ_1, ϕ_2 signify the volume fractions of Cu and Al_2O_3 and similarly for other quantities with suffixes 1 and 2. Also, κ_{nf} and κ_f denote the thermal conductivities of Cu nanofluid and water, respectively. The physical properties of water, Cu and Al_2O_3 are stated in Table 1.

The governing PDEs are converted into ODEs by using suitable transformations and stream function ψ as $u = \frac{\partial\psi}{\partial y}$ and $v = -\frac{\partial\psi}{\partial x}$ (Ref. 51),

$$\zeta = y\sqrt{\frac{(m+1)U_0(x+b)^{m-1}}{2\nu_f(1-\alpha t)}}, \quad \psi = \sqrt{\frac{2\nu_f U_0(x+b)^{m+1}}{(m+1)(1-\alpha t)}}F(\zeta), \quad (7)$$

$$\Theta(\zeta) = \frac{(T - T_\infty)}{(T_w - T_\infty)}, \quad \Phi(\zeta) = \frac{(C - C_\infty)}{(C_w - C_\infty)}, \quad (8)$$

where ζ is a variable and ν_f is the kinematic viscosity of fluid. The continuity equation (1) is automatically satisfied for the above-considered transformations. And the remaining transformed system of ODEs is of the form

$$\frac{1}{\varphi_1} F''' - \frac{2m}{m+1} F'^2 + FF'' - \frac{2A}{m+1} \left(F' + \frac{\zeta}{2} F'' \right) = 0, \quad (9)$$

$$\begin{aligned} \frac{\kappa_{\text{hnf}}/\kappa_f}{\varphi_2} \Theta'' + \text{Pr} \left[\text{Nb}\Theta'\Phi' + \text{Nt}\Theta'^2 - \left(\frac{2}{m+1} \right) \left\{ A \left(\frac{\zeta}{2} \Theta' + \Theta_n \right) \right. \right. \\ \left. \left. + \left(\frac{1-m}{2} \right) F'\Theta - \left(\frac{m+1}{2} \right) F\Theta' \right\} \right] = 0, \end{aligned} \quad (10)$$

Table 1. The physical properties of water, Cu and Al_2O_3 .³⁰

Property	Water	Cu	Al_2O_3
ρ (kg m ⁻³)	997.1	8933	3970
κ (Wm ⁻¹ K ⁻¹)	0.613	401	40
c_p (J kg ⁻¹ K ⁻¹)	4179	385	765

$$\Phi'' + \frac{Nt}{Nb} \Theta'' - Sc \left(\frac{2}{m+1} \right) \left[A \left(\Phi n + \frac{\zeta}{2} \Phi' \right) + \left(\frac{1-m}{2} \right) F' \Phi - \left(\frac{m+1}{2} \right) F \Phi' \right] = 0, \tag{11}$$

where the parameters A , Pr , Nt , Nb and Sc denote unsteadiness parameter, Prandtl number, thermophoresis parameter, Brownian motion parameter and Schmidt number, respectively. And all the above-described parameters are defined as follows:

$$\left. \begin{aligned} \varphi_1 &= (1 - \phi_1)^{2.5} (1 - \phi_2)^{2.5} \left\{ (1 - \phi_2) \left[(1 - \phi_1) + \phi_1 \frac{\rho_1}{\rho_f} \right] + \phi_2 \frac{\rho_2}{\rho_f} \right\}, \\ A &= \frac{\alpha}{U_0(x+b)^{m-1}}, \quad \varphi_2 = \frac{(\rho c_p)_{hnf}}{(\rho c_p)_f} = \left\{ (1 - \phi_2) \left[(1 - \phi_1) + \phi_1 \frac{(\rho c_p)_1}{(\rho c_p)_f} \right] + \phi_2 \frac{(\rho c_p)_2}{(\rho c_p)_f} \right\}, \\ Pr &= \frac{\nu_f}{(\kappa_f / (\rho c_p)_f)}, \quad Nb = \frac{\tau D_B (C_w - C_\infty)}{\nu_f}, \quad Nt = \frac{\tau D_T (T_w - T_\infty)}{T_\infty \nu_f}, \quad Sc = \frac{\nu_f}{D_B}, \end{aligned} \right\} \tag{12}$$

along with the associated transformed boundary conditions

$$\left. \begin{aligned} F(\chi) &= \chi \frac{1-m}{1+m}, \quad F'(\chi) = 1, \quad \Theta(\chi) = 1, \quad \Phi(\chi) = 1, \\ F'(\chi) &\rightarrow 0, \quad \Theta(\chi) \rightarrow 0, \quad \Phi(\chi) \rightarrow 0 \quad \text{as } \chi \rightarrow \infty. \end{aligned} \right\} \tag{13}$$

Here $\chi = B \sqrt{\frac{U_0(m+1)}{2\nu_f}}$ is the wall thickness parameter of the horizontal upper parabolic surface. φ_1 and φ_2 are nanoparticle's volume fraction-related parameters. The boundary restriction of the problem is confined to the domain $[\chi, \infty)$. So, we define $F(\zeta - \chi) = f(\eta)$, $\Theta(\zeta - \chi) = \theta(\eta)$ and $\Phi(\zeta - \chi) = \phi(\eta)$ to convert the computational domain from $[\chi, \infty)$ to $[0, \infty)$, which gives

$$\frac{1}{\varphi_1} f''' - \frac{2m}{m+1} f'^2 + f f'' - \frac{2A}{m+1} \left(f' + \frac{\eta}{2} f'' \right) = 0, \tag{14}$$

$$\begin{aligned} \frac{\kappa_{hnf}/\kappa_f}{\varphi_2} \theta'' + Pr \left[Nb \theta' \phi' + Nt \theta'^2 - \left(\frac{2}{m+1} \right) \left\{ A \left(\frac{\eta}{2} \theta' + \theta n \right) \right. \right. \\ \left. \left. + \left(\frac{1-m}{2} \right) f' \theta - \left(\frac{m+1}{2} \right) f \theta' \right\} \right] = 0, \end{aligned} \tag{15}$$

$$\phi'' + \frac{Nt}{Nb} \theta'' - Sc \left(\frac{2}{m+1} \right) \left[A \left(\phi n + \frac{\eta}{2} \phi' \right) + \left(\frac{1-m}{2} \right) f' \phi - \left(\frac{m+1}{2} \right) f \phi' \right] = 0, \tag{16}$$

with the boundary conditions

$$\left. \begin{aligned} f(0) &= \chi \frac{1-m}{1+m}, \quad f'(0) = 1, \quad \theta(0) = 1, \quad \phi(0) = 1, \\ f'(\eta) &\rightarrow 0, \quad \theta(\eta) \rightarrow 0, \quad \phi(\eta) \rightarrow 0 \quad \text{as } \eta \rightarrow \infty. \end{aligned} \right\} \tag{17}$$

Now, the local skin friction coefficient C_{fr} , local Nusselt number Nu_x and local Sherwood number Sh_x , which are very relevant quantities in engineering problems, are expressed as⁴⁹

$$C_{fr} = \frac{\tau_w}{\rho_f u_w^2}, \quad Nu_x = \frac{(x+b)}{\kappa_f} \frac{q_w}{(T_w - T_\infty)}, \quad Sh_x = \frac{(x+b)}{D_B} \frac{q_m}{(C_w - C_\infty)}, \quad (18)$$

where τ_w is the wall shear stress, q_w is heat transfer rate and q_m is mass transfer rate at the surface, which are defined as

$$\begin{aligned} \tau_w &= \mu_{hnf} \left(\frac{\partial u}{\partial y} \right)_{y=B(x+b)^{\frac{1-m}{2}}}, & q_w &= -\kappa_{hnf} \left(\frac{\partial T}{\partial y} \right)_{y=B(x+b)^{\frac{1-m}{2}}}, \\ q_m &= -D_B \left(\frac{\partial C}{\partial y} \right)_{y=B(x+b)^{\frac{1-m}{2}}}. \end{aligned} \quad (19)$$

Using (7), (8) and (19), we get from (18)

$$\left. \begin{aligned} C_{fr} Re_x^{1/2} &= \frac{1}{(1-\phi_1)^{2.5}(1-\phi_2)^{2.5}} \sqrt{\frac{m+1}{2}} f''(0), \\ Nu_x / Re_x^{1/2} &= -\frac{\kappa_{hnf}}{\kappa_f} \sqrt{\frac{m+1}{2}} \theta'(0), \\ Sh_x / Re_x^{1/2} &= -\sqrt{\frac{m+1}{2}} \phi'(0), \end{aligned} \right\} \quad (20)$$

where $Re_x = u_w(x+b)/\nu_f$ is the local Reynolds number.

3. Numerical Method and Its Validation

The governing system of coupled nonlinear ODEs of the above-mentioned physical problem is solved with the help of ‘‘Keller-box’’ method^{57–59} executed in MATLAB software by converting the boundary value problem into a system of first-order ODEs. The advantage of this numerical technique is in its unconditional stability and easy computational procedure. This method has second-order accuracy. To apply this computation method, the main steps are as follows:

- (a) Convert higher-order ODEs to a system of first-order ODEs, and the transformed equations are given by

$$\left. \begin{aligned} f' &= p, & p' &= q, & \theta' &= r, & \phi' &= s, \\ q' &= \varphi_1 \left[\frac{2m}{m+1} p^2 - fq + \frac{2A}{m+1} \left(p + \frac{\eta}{2} q \right) \right], \\ r' &= -Pr \frac{\varphi_2}{\kappa_{hnf}/\kappa_f} \left[Nbrs + Ntr^2 - \left(\frac{2}{m+1} \right) \left\{ A \left(\frac{\eta}{2} r + \theta n \right) \right. \right. \\ &\quad \left. \left. + \left(\frac{1-m}{2} \right) p\theta - \left(\frac{m+1}{2} \right) fr \right\} \right], \\ s' &= -\frac{Nt}{Nb} r' + Sc \left(\frac{2}{m+1} \right) \left[A \left(\phi n + \frac{\eta}{2} s \right) + \left(\frac{1-m}{2} \right) p\phi - \left(\frac{m+1}{2} \right) fs \right], \end{aligned} \right\} \quad (21)$$

along with the boundary restrictions

$$\left. \begin{aligned} f(0) &= \chi \frac{1-m}{1+m}, \quad p(0) = 1, \quad \theta(0) = 1, \quad \phi(0) = 1, \\ p(\eta) &\rightarrow 0, \quad \theta(\eta) \rightarrow 0, \quad \phi(\eta) \rightarrow 0 \quad \text{as } \eta \rightarrow \infty. \end{aligned} \right\} \quad (22)$$

- (b) To discretize the converted equations, central difference formulas have been used. The functions and their derivatives with respect to η at midpoint $(x^i, \eta_{j-1/2})$ are replaced by

$$(u)_{j-1/2}^i = \frac{1}{2}[(u)_j^i + (u)_{j-1}^i] \quad \text{and} \quad \left(\frac{\partial u}{\partial \eta}\right)_{j-1/2}^i = \frac{u_j^i - u_{j-1}^i}{h_j},$$

where h_j is the step size. After using the above relations, we will get a system of nonlinear equations.

- (c) Since the obtained set of algebraic equations are in a nonlinear form, so Newton’s method is used to linearize those equations.
 (d) Now, write these linear equations in matrix vector form $[A][\delta] = [r]$, where $[A]$ is the block-tridiagonal matrix, $[r]$ is a known vector and $[\delta]$ is an unknown vector.
 (e) Finally, the system $[A][\delta] = [r]$ is solved by the LU decomposition method. In this particular scheme, we represent $[A]$ in the form of a product of lower and

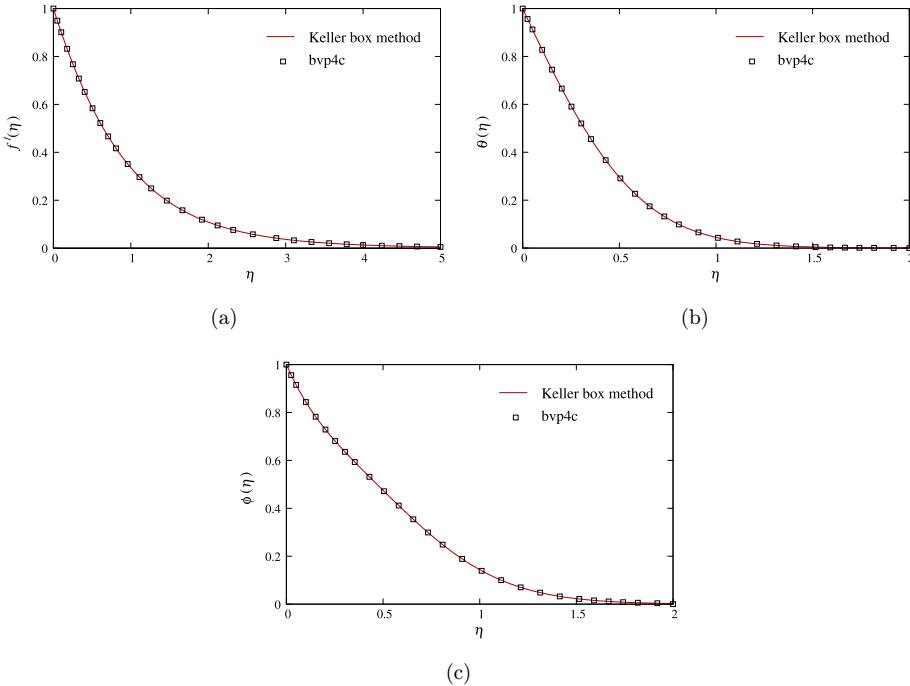


Fig. 2. (Color online) Comparison between the “Keller-box” and “bvp4c” methods for (a) velocity, (b) temperature and (c) concentration with fixed values of the parameters namely $A = 0.1$, $Nb = 0.1$, $Nt = 0.2$, $n = 0.5$, $m = 0.25$, $Pr = 6.8$, $Sc = 7$, $\phi_1 = \phi_2 = 0.03$ and $\chi = 0.3$.

upper triangular matrices, i.e., $[A] = [L][U]$. Hence, the problem becomes $[L][U][\delta] = [r]$.

Now, if we suppose $[U][\delta] = [z]$, this implies that after solving the reduced system $[L][z] = [r]$, where $[L]$ and $[r]$ are known vectors, we get the value of $[z]$. And after that, putting $[z]$ in $[U][\delta] = [z]$, we can find the required values.

And these calculations are repeated until the assumed convergence criterion is satisfied and we stop the calculations when the gaps between the values calculated at two alternative levels are less than ε , where ε is a very small value taken to be: $\varepsilon = 0.00001$. A more detailed interpretation of numerical computation procedure with data collection and processing description inside the “Keller-box” method can be found in the work by Jamshed *et al.*⁵⁹ Graphical comparisons of the numerical results for velocity, temperature and concentration obtained using the “Keller-box” method and MATLAB solver “bvp4c”^{60–62} are presented in Figs. 2(a)–2(c), for the fixed values of parameters. These figures show that the obtained profiles by the two methods are almost similar. The precision of our reported results is verified by comparing them with the solutions reported by Wang,⁶³ Gorla and Sidawi⁶⁴ and Khan and Pop⁶⁵ for several values of Pr and Nt in Tables 2 and 3. We have found a great agreement between solutions found in earlier articles and our results computed by the “Keller-box” method and “bvp4c” solver.

Table 2. Comparison of results for the local Nusselt number ($Nu_x Re_x^{-1/2}$) when $m = 1$ and $Nb = Nt = A = \phi_1 = \phi_2 = n = \chi = 0$.

Pr	Wang ⁶³	Gorla and Sidawi ⁶⁴	Khan and Pop ⁶⁵	Our results	
				bvp4c	KBM
0.07	0.0656	0.0656	0.0656	0.06568362	0.06568381
0.20	0.1691	0.1691	0.1691	0.16914717	0.16914718
0.70	0.4539	0.5349	0.4539	0.45391665	0.45391815
2	0.9114	0.9114	0.9113	0.91135768	0.91131629
7	1.8954	1.8954	1.8954	1.89540328	1.89531752
20	3.3539	3.3539	3.3539	3.35390451	3.35375450
70	6.4622	6.4622	6.4621	6.46220155	6.46222038

Table 3. Comparison table when $A = 0$, $Nb = 0.1$, $n = 0$, $m = 1$, $Pr = 10$, $Sc = 10$, $\phi_1 = \phi_2 = 0$ and $\chi = 0$.

Nt	Khan and Pop ⁶⁵		Our results by “bvp4c”		Our results by KBM	
	$Nu_x Re_x^{-1/2}$	$Sh_x Re_x^{-1/2}$	$Nu_x Re_x^{-1/2}$	$Sh_x Re_x^{-1/2}$	$Nu_x Re_x^{-1/2}$	$Sh_x Re_x^{-1/2}$
0.1	0.9524	2.1294	0.95237698	2.12939366	0.95237414	2.12926805
0.2	0.6932	2.2740	0.69317663	2.27401778	0.69318198	2.27386804
0.3	0.5201	2.5286	0.52007903	2.52863829	0.52008900	2.52846827
0.4	0.4026	2.7952	0.40258076	2.79517009	0.40259112	2.79499159
0.5	0.3211	3.0351	0.32105466	3.03514153	0.32106395	3.03496212

4. Results and Discussion

In this section, the impacts of the flow dynamics ruling parameters involved in flow-governing reduced system of ODEs [Eqs. (14)–(16)] are described through graphs and tables. From Figs. 3–6, we have inferred about some important physical quantities, viz. surface drag force, heat and mass transfer rates, from the application prospects in several industrial processes. Also, the influences of aforesaid parameters on flow field, energy and mass distributions are shown in Figs. 7–14. If the volume fraction of any one nanoparticle is considered to be zero then the hybrid nanofluid reduces to a mono-nanofluid. Here, $\phi_1 = 0$ and $\phi_2 = 0$ correspond to $\text{Al}_2\text{O}_3/\text{water}$ and Cu/water nanofluids, respectively. For parabolic surfaces m is restricted to be less than 1, so the boundary condition $f(0) = \chi^{\frac{1-m}{1+m}}$ specified in Eq. (17) is mathematically equivalent to $f(0) > 0$. The parametric values $A = 0.1$, $\text{Nb} = 0.1$, $\text{Nt} = 0.2$, $n = 0.5$, $m = 0.25$, $\text{Pr} = 6.8$, $\text{Sc} = 7$, $\phi_1 = \phi_2 = 0.03$ and $\chi = 0.3$ (where ϕ_1 and ϕ_2 are the volume fraction parameters for Cu and Al_2O_3 nanoparticles, respectively) are kept fixed throughout the computation; else, it is specified when their variations are taken into consideration in figures or tables.

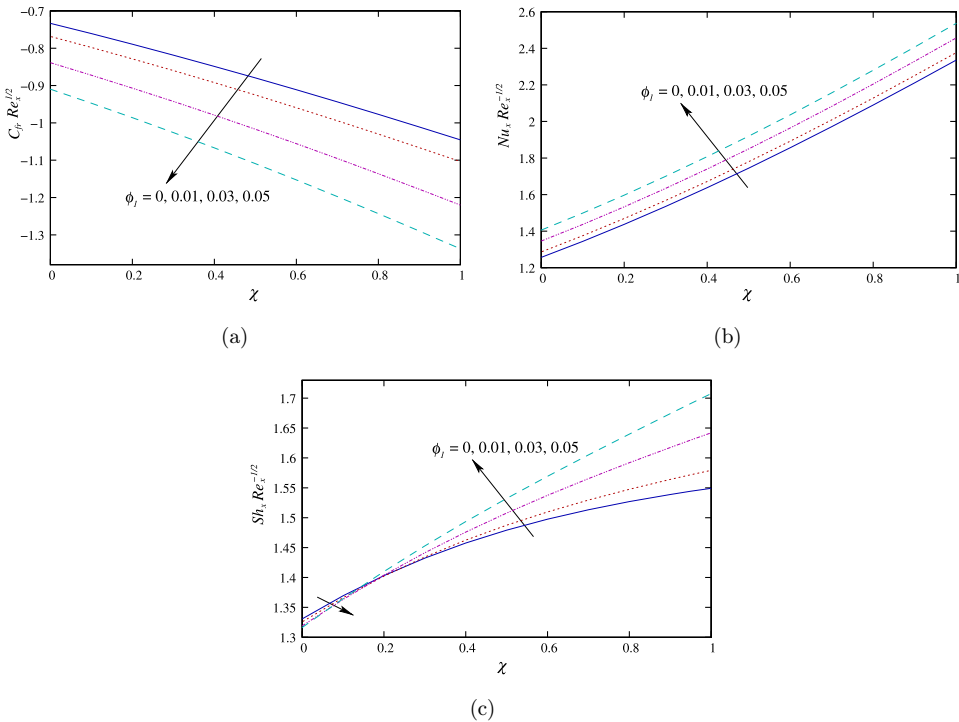


Fig. 3. (Color online) Effects of Cu nanoparticles' volume on the (a) skin friction coefficient, (b) Nusselt number and (c) Sherwood number versus the wall thickness parameter with $A = 0.1$, $\text{Nb} = 0.1$, $\text{Nt} = 0.2$, $n = 0.5$, $m = 0.25$, $\text{Pr} = 6.8$, $\text{Sc} = 7$, $\phi_1 = 0.03$ and $\chi = 0.3$.

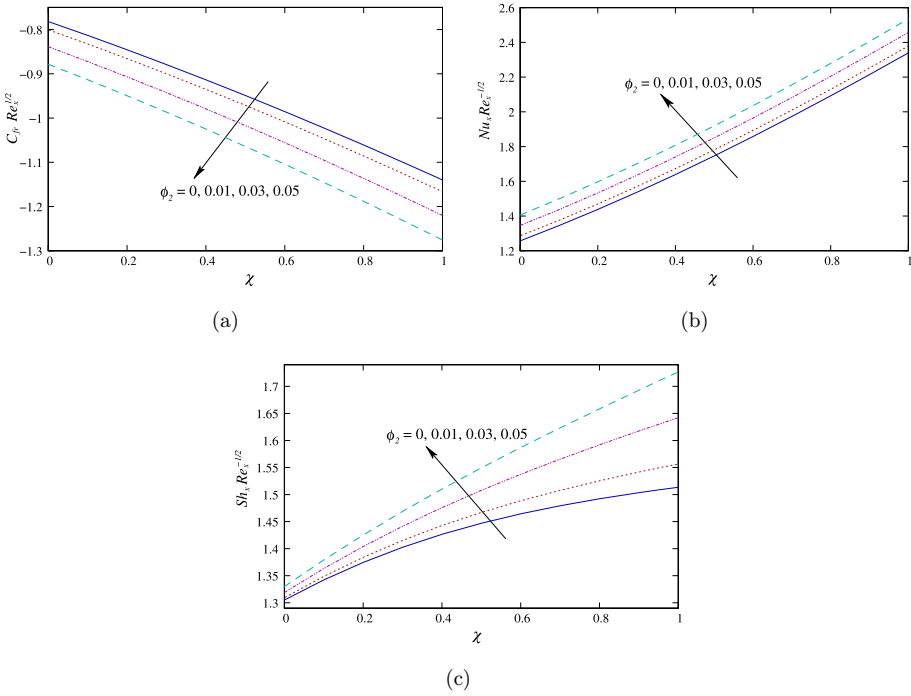


Fig. 4. (Color online) Effects of alumina nanoparticles' volume on the (a) skin friction coefficient, (b) Nusselt number and (c) Sherwood number versus the wall thickness parameter with $A = 0.1$, $Nb = 0.1$, $Nt = 0.2$, $n = 0.5$, $m = 0.25$, $Pr = 6.8$, $Sc = 7$, $\phi_2 = 0.03$ and $\chi = 0.3$.

4.1. Variations in surface drag, heat and mass transfer rates

A comparison table of percentage increments in the surface drag force and heat transfer rate with base fluid water, for the different volume fractions of hybrid nanofluid constituents, is provided in Table 4. Following are the important findings

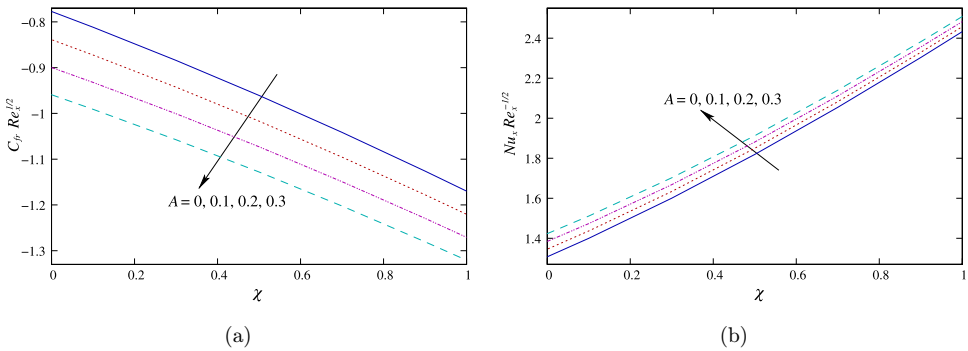


Fig. 5. (Color online) Effects of unsteadiness on the (a) skin friction coefficient, (b) Nusselt number and (c) Sherwood number versus the wall thickness parameter with $Nb = 0.1$, $Nt = 0.2$, $n = 0.5$, $m = 0.25$, $Pr = 6.8$, $Sc = 7$, $\phi_1 = \phi_2 = 0.03$ and $\chi = 0.3$.

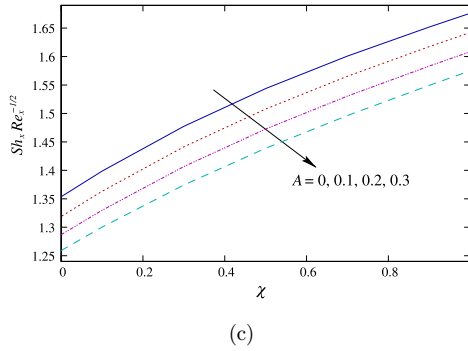


Fig. 5. (Continued)

that may be derived by analyzing the table:

- (i) If we consider more Cu nanoparticles than alumina, then it results in larger enhancement of surface drag along with the heat transfer rate, whereas a higher amount of alumina produces an approximately similar cooling rate with less surface drag.
- (ii) Also, the suspension cost of nanocomposite may be reduced by choosing suitable amounts of two types of nanoparticles with approximately equal surface cooling rates.
- (iii) So, a smart combination of volumes of Cu and Al_2O_3 nanoparticles will achieve higher cooling rate and lower surface drag with the desired cost efficiency.
- (iv) Moreover, maximum improvements in surface drag and rate of heat transport are noted for $\phi_1 = \phi_2 = 0.05$, which are 41.8% and 22.7% higher to water, respectively.

The impacts of nanoparticles (Cu and Al_2O_3) of the hybrid nanocomposite on the surface drag, heat and mass transfer rates are portrayed in Figs. 3 and 4 depending

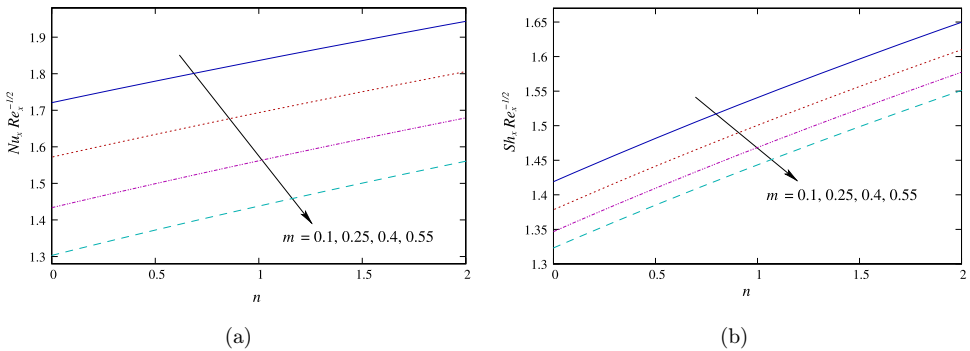


Fig. 6. (Color online) Effects of power-law exponent on the (a) Nusselt number and (b) Sherwood number versus n with $A = 0.1$, $Nb = 0.1$, $Nt = 0.2$, $n = 0.5$, $Pr = 6.8$, $Sc = 7$, $\phi_1 = \phi_2 = 0.03$ and $\chi = 0.3$.

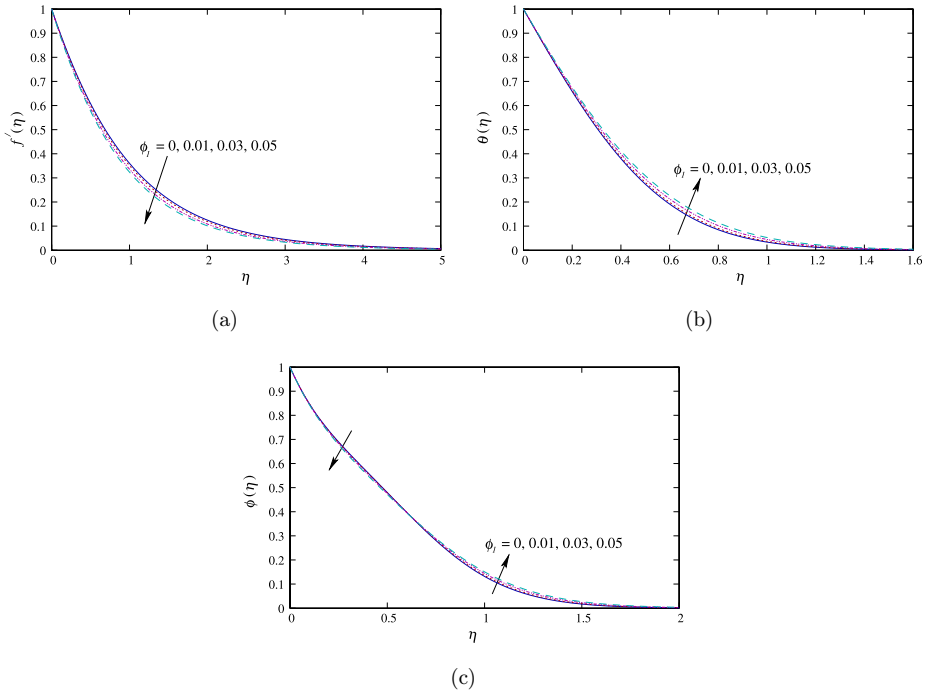


Fig. 7. (Color online) Impacts of Cu nanoparticles' volume on the (a) velocity, (b) temperature and (c) concentration with $A = 0.1$, $Nb = 0.1$, $Nt = 0.2$, $n = 0.5$, $m = 0.25$, $Pr = 6.8$, $Sc = 7$, $\phi_1 = 0.03$ and $\chi = 0.3$.

on the quantity of nanoparticle loadings. We can observe that as the volume fraction of particles increases, the surface exerts more drag on the fluid and vice versa. Surface drag is dependent on the type of nanoparticles due to their varying physical properties. If we consider alumina/water nanofluid and later on if certain fractions of Cu

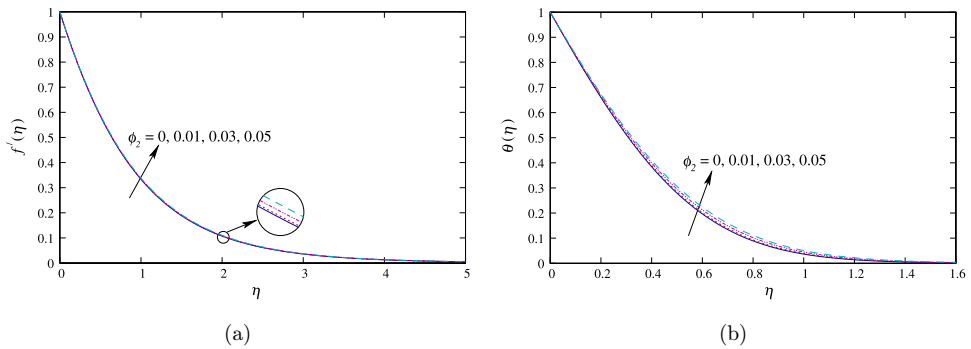


Fig. 8. (Color online) Impacts of alumina nanoparticles' volume on the (a) velocity, (b) temperature and (c) concentration with $A = 0.1$, $Nb = 0.1$, $Nt = 0.2$, $n = 0.5$, $m = 0.25$, $Pr = 6.8$, $Sc = 7$, $\phi_2 = 0.03$ and $\chi = 0.3$.

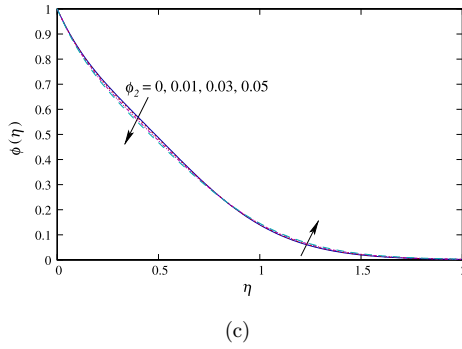


Fig. 8. (Continued)

nanoparticles are to be added, then the growth of drag force is more (because of the nanoparticles with higher density) than what we get by taking the opposite combination to form a hybrid nanofluid, i.e., dispersion of alumina particles in Cu/water nanofluid. Also, thickness of the surface may be considered as another factor that affects the engineering quantities, like drag, heat and mass transfer rates. Surface

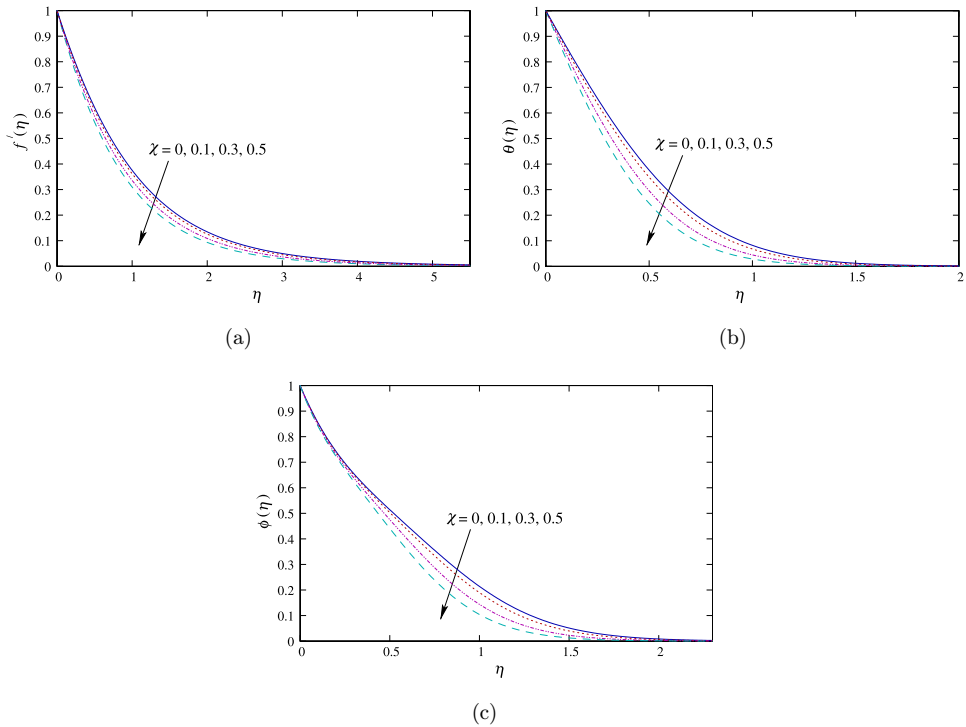


Fig. 9. (Color online) Impacts of wall thickness parameter on the (a) velocity, (b) temperature and (c) concentration with $A = 0.1$, $Nb = 0.1$, $Nt = 0.2$, $n = 0.5$, $m = 0.25$, $Pr = 6.8$, $Sc = 7$ and $\phi_1 = \phi_2 = 0.03$.

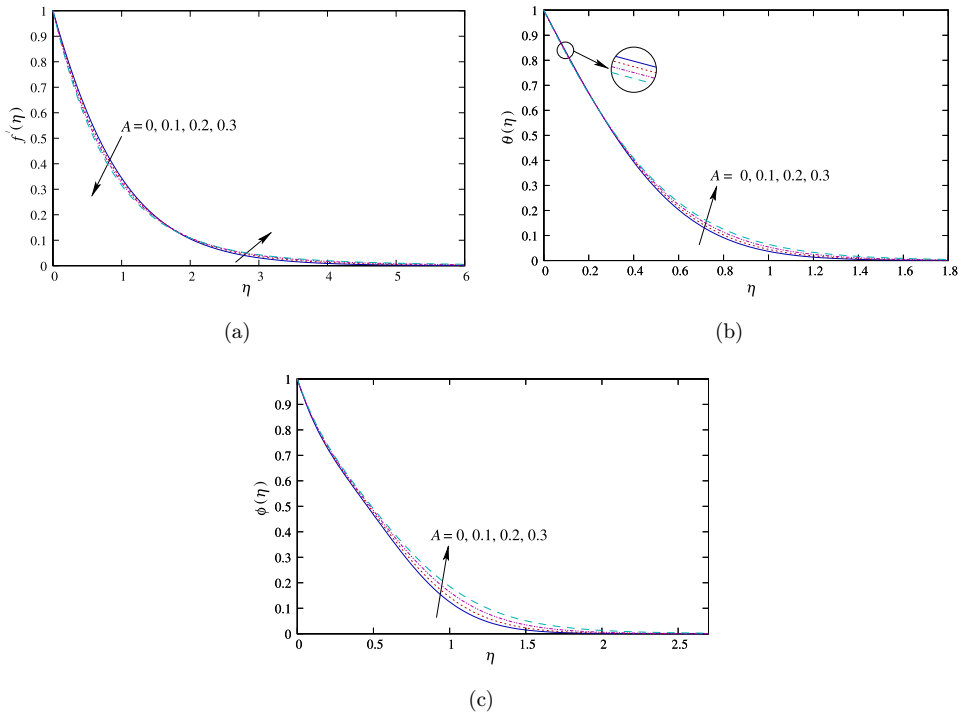


Fig. 10. (Color online) Effects of unsteadiness on the (a) velocity, (b) temperature and (c) concentration with $Nb = 0.1$, $Nt = 0.2$, $n = 0.5$, $m = 0.25$, $Pr = 6.8$, $Sc = 7$, $\phi_1 = \phi_2 = 0.03$ and $\chi = 0.3$.

heat transfer rate enhances significantly for hybrid nanofluid with the nanoparticle concentration. So, a warm surface cools down quickly by using hybrid nanofluids as a heat transfer medium. Because of the superior physical properties of nanoparticles, i.e., thermal conductivity and heat capacity, both heat transfer mechanisms (i.e., conduction and convection) enhance and consequently, the heat transport rate becomes higher from the surface. Transportation of mass shows a significantly distinct character in response to increasing the nanoparticles' volume fractions. This different nature depends on the nanoparticle and its thermo-physical properties. For the suspension of Cu in 3 vol.% of Al_2O_3 /water nanofluid, mass transfer rate at the surface decreases with nanoparticle concentration for thinner surface, i.e., it is valid for a slender parabolic surface. But, a contrasting trend has been noticed for a thicker surface. On the other hand, when we add Al_2O_3 to 3 vol.% of Cu in water, a uniform nature of mass transfer rate (rising with the concentration of nanoparticles) is observed without any restriction on the surface thickness. This means that for thicker parabolic surfaces transportation of mass is faster with both Cu and Al_2O_3 volume fractions. In short, thinner surfaces create less drag as compared to thicker surfaces, so thinner surfaces may be considered to prevent the losses due to extra drag force on the surface, which is an important characteristic for many industrial applications.

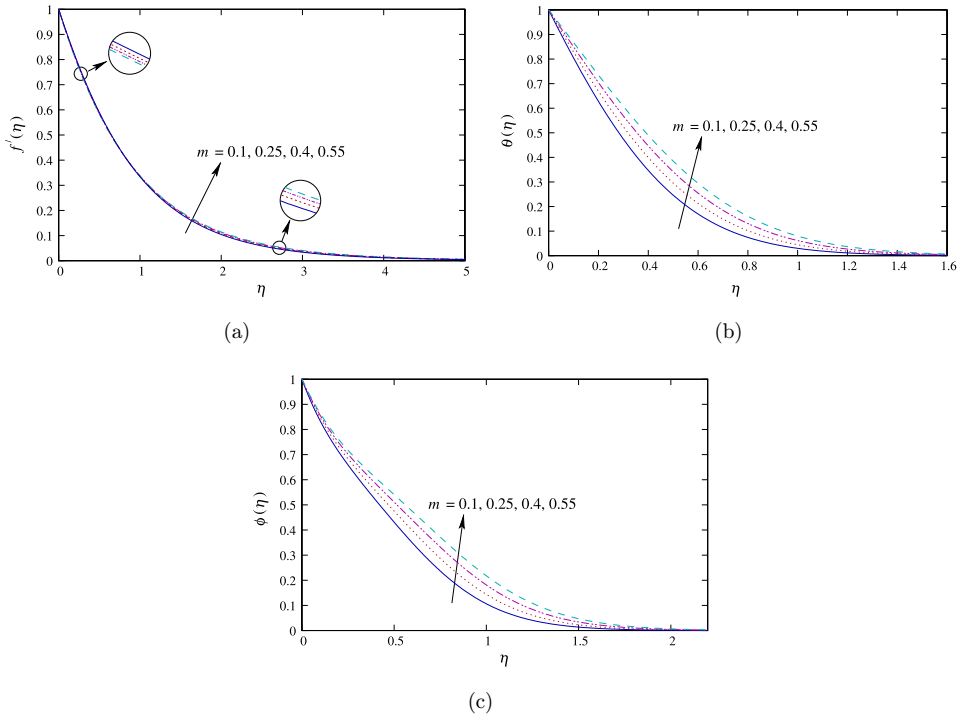


Fig. 11. (Color online) Effects of power-law exponent on the (a) velocity, (b) temperature and (c) concentration with $A = 0.1$, $Nb = 0.1$, $Nt = 0.2$, $n = 0.5$, $Pr = 6.8$, $Sc = 7$, $\phi_1 = \phi_2 = 0.03$ and $\chi = 0.3$.

Figure 5 portrays the consequences of unsteadiness on the flow field drag along with heat and mass transports. The unsteadiness in the flow creates an additional amount of drag as compared to a steady flow. Also, it is observed that the rate of heat transfer at the surface exhibits an enhancing trend with unsteadiness. Physically,

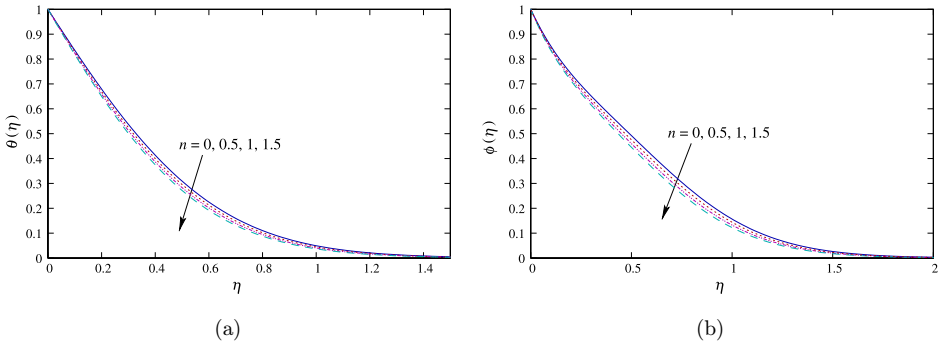


Fig. 12. (Color online) Effects of power-law index on the (a) temperature and (b) concentration with $A = 0.1$, $Nb = 0.1$, $Nt = 0.2$, $m = 0.25$, $Pr = 6.8$, $Sc = 7$, $\phi_1 = \phi_2 = 0.03$ and $\chi = 0.3$.

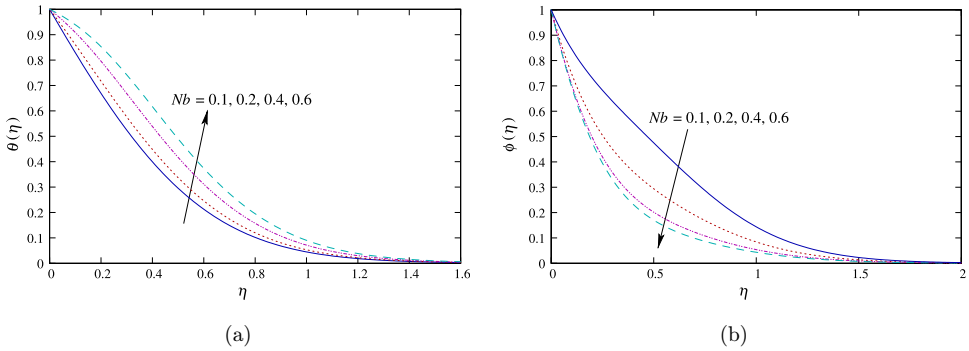


Fig. 13. (Color online) Effects of Brownian motion on the (a) temperature and (b) concentration with $A = 0.1$, $Nt = 0.2$, $n = 0.5$, $m = 0.25$, $Pr = 6.8$, $Sc = 7$, $\phi_1 = \phi_2 = 0.03$ and $\chi = 0.3$.

this fact indicates a faster cooling of the heated surface for larger values of unsteadiness. With the consideration of unsteadiness, it may be determined that the cooling of a warm surface will take less time in comparison to a steady flow. An increase in unsteadiness retards the mass transfer rate at the surface. Unsteadiness parameter, A , is directly proportional to the time controlling factor α , so α rises with A and hence the flow becomes more time-dependent causing less drag force and less nano-mass transport with high cooling rate.

Physically, the conditions $m = 1$ and $n = 0$ correspond to the nanofluid flow with constant wall temperature and concentration, while $n = 0$ indicates the situation where temperature and concentration of nanoparticles at the wall only depend on the space variable, but not on the time scale. Figure 6 presents the influence of m and n on the heat and mass transfer rates. The impacts of m on heat and mass transfer rates are similar, and for the same scenario an opposite influence for n is witnessed, i.e., both rates reduce with m and rise with n . Thus, we can say that, from a practical viewpoint, surface cooling is faster for low power-law exponent (m) and high power-law index (n). With increasing m the wall distributions of temperature and

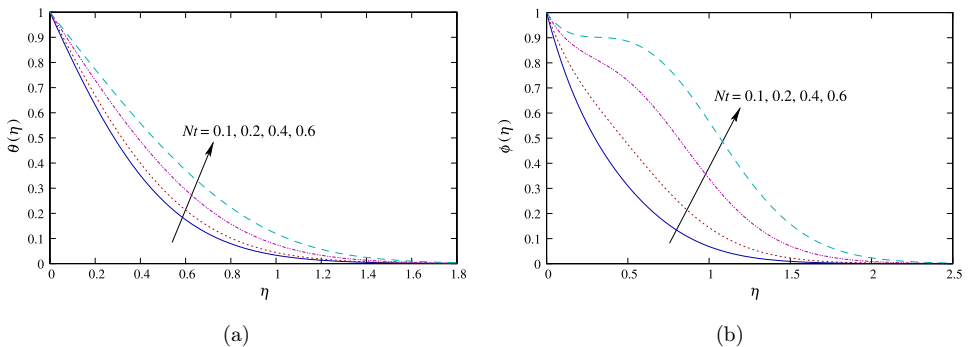


Fig. 14. (Color online) Effects of thermophoresis on the (a) temperature and (b) concentration with $A = 0.1$, $Nb = 0.1$, $n = 0.5$, $m = 0.25$, $Pr = 6.8$, $Sc = 7$, $\phi_1 = \phi_2 = 0.03$ and $\chi = 0.3$.

Table 4. Surface drag forces and heat transfer rates for different values of nanoparticle volume fractions.

ϕ_1	ϕ_2	$C_{fr}Re_x^{1/2}$	$Nu_xRe_x^{-1/2}$	Percentages of increment in comparison with water	
				$C_{fr}Re_x^{1/2}$	$Nu_xRe_x^{-1/2}$
0	0	-0.75459285	1.44007394	0%	0%
0.01	0.01	-0.81709331	1.50402728	8.282673232%	4.440976%
	0.02	-0.83831099	1.53604339	11.09447830%	6.664203%
	0.03	-0.85986819	1.56815860	13.95127717%	8.894311%
	0.04	-0.8817807	1.60038160	16.85516236%	11.13190%
	0.05	-0.90406481	1.63272138	19.80829264%	13.37761%
0.03	0.01	-0.89996704	1.56867825	19.26524880%	8.930396%
	0.02	-0.92106967	1.60132469	22.06180724%	11.19739%
	0.03	-0.9425390	1.63407377	24.90706743%	13.47152%
	0.04	-0.96439263	1.66693452	27.80304372%	15.75340%
	0.05	-0.98664394	1.69991631	30.75182729%	18.04368%
0.05	0.01	-0.98326631	1.63338759	30.3042177%	13.42387%
	0.02	-1.00437590	1.66666419	33.10169849%	15.73463%
	0.03	-1.02587578	1.70004692	35.9509012%	18.05275%
	0.04	-1.04778100	1.73354520	38.85382031%	20.37890%
	0.05	-1.07010722	1.76716873	41.81253109%	22.71375%
0.02	0.01	-0.85851406	1.53635318	13.77182543%	6.685715%
	0.04	-0.94152829	1.60101784	24.77302031%	11.17609%
0.02	0.03	-0.90115418	1.60111679	19.42257073%	11.18296%
0.04		-0.98409298	1.66704517	30.41376949%	15.76108%
0.02	0.05	-0.94527393	1.66631965	25.26939925%	15.71070%
0.04		-1.02823611	1.73352727	36.26369638%	20.37766%

concentration become weak and accordingly, it produces drops of heat and mass transports.

4.2. Variations in velocity, temperature and concentration

The variations in hybrid nanofluid velocity with different amounts of one of the two nanoparticle concentrations (0%, 1%, 3% and 5%), while the other nanoparticle's quantity is fixed (3%), are shown in Figs. 7(a) and 8(a). The velocity of Al₂O₃/water is higher than the hybrid nanofluid by adding a certain amount of Cu. This means that a hybrid nanofluid with a larger amount of Cu has a slower speed because for higher concentration of Cu more drag appears in the fluid, which creates resistance to the fluid motion and hence reduces the nanofluid velocity with Cu loading. By contrast, when Cu/water nanofluid is considered with the suspension of Al₂O₃ nanoparticles making a hybrid nanofluid, the velocity of the resultant hybrid fluid shows minute growth due to more collisions between nanoparticles for lower density of Al₂O₃. Figures 7(b), 7(c) and 8(b), 8(c) show the impacts of the quantities of nanoparticles (Cu and Al₂O₃) used as components of the total nanoparticle volume fraction on the nanofluid temperature and concentration distributions, respectively. The temperature and concentration of the modeled hybrid nanofluid behave in the

same manner for mixing some amount of one nanoparticle into another nanofluid. Nanofluid's temperature becomes high with rising percentages of both nanoparticles and it occurs because of the joint impact of the higher thermal conductivities of Cu and Al₂O₃ solid particles and the convection character inside the flow. Also, the concentration of the hybrid nanofluid near the sheet decays, but an opposite nature is noticed far from the surface. These effects are prominent adjacent to and far away from the surface for suspensions of Al₂O₃ and Cu particles, respectively.

From Fig. 9, the influences of surface thickness on the hybrid nanofluid flow properties (viz. velocity, temperature and concentration) may be witnessed. These figures indicate that depletions in the boundary layer thicknesses (BLTs) associated with momentum, temperature and concentration are caused with the thickness parameter χ . A larger thickness of the surface, i.e., a greater value of χ at the boundary condition, corresponds to the position under which the surface becomes close to the ambient fluid layers and as a result, the thicknesses of the various boundary layers become smaller.

The variations in several physical properties for multiple values of unsteadiness parameter are elucidated in Fig. 10. These figures describe the decaying velocity and temperature near the surface, but show the opposite nature far from it. This happens due to the continuous dependence of wall temperature and wall velocity on the time variable, i.e., the velocity and temperature increase with time near the wall, but the impacts of time-dependent wall temperature and wall velocity diminish as the distance from the surface becomes large and in that portion the flow unsteadiness becomes prominent over the time dependency of wall conditions. As a consequence, greater thicknesses of the boundary layers are encountered. Also, unsteadiness increases the concentration BLT.

Figure 11(a) exhibits a perfect picture of the fluctuating nature of velocity for different power-law exponent (m) values, i.e., the velocity at a point near the wall reduces, while it enlarges after some distance from the boundary surface. The temperature and concentration of hybrid nanofluid show a similar behavior, i.e., both quantities augment for various values of the power-law exponent which are exhibited in Figs. 11(b) and 11(c). A change in power-law exponent causes space-dependent changes in the boundary conditions, which produce a rise of velocity, temperature and concentration. In Figs. 12(a) and 12(b), the impacts of power-law index (n) on the temperature and concentration fields of the considered nanofluid are explained. The temperature and concentration of hybrid nanofluid decay with n , and as a consequence their respective BLTs reduce.

Figures 13 and 14 exhibit the influence of Brownian motion and thermophoresis on the temperature and nanoparticle concentration fields. Temperature and its associated BLT enhance due to the occurrence of these two physical phenomena, i.e., Nb and Nt. From Fig. 13(b), a noticeable change in nanoparticle concentration can be observed for low intensity of random motion. As the Brownian motion of nanoparticles increases, the above change becomes lighter, i.e., the nanoparticle concentration decays. Physically, Brownian motion works to heat the boundary layer

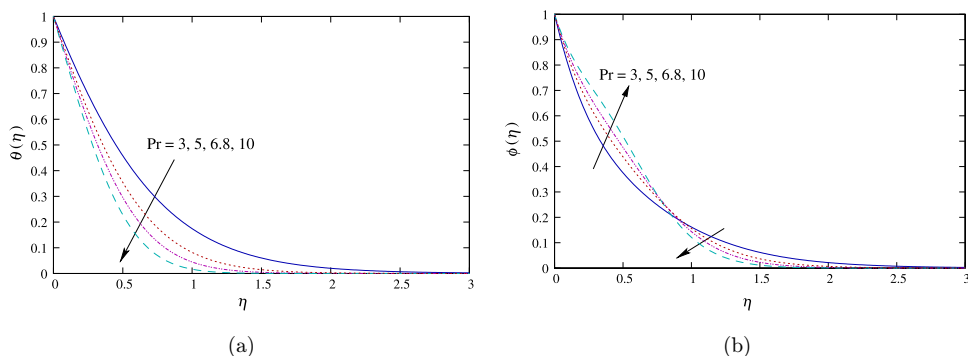


Fig. 15. (Color online) Effects of Prandtl number on the (a) temperature and (b) concentration with $A = 0.1$, $Nb = 0.1$, $Nt = 0.2$, $n = 0.5$, $m = 0.25$, $Sc = 7$, $\phi_1 = \phi_2 = 0.03$ and $\chi = 0.3$.

because the frequency of collisions between particles enhances with larger values of Nb . Figure 14(b) indicates an increase in nanoparticle concentration with thermophoresis. Under the thermophoresis effect, temperature gradient force causes the nanoparticles to move from hotter region to colder region, which is the reason behind the temperature drop with Nt .

Figure 15 displays the impact of variations of Pr on the temperature and concentration profiles. Larger Pr shortens the thickness of both boundary layers due to large momentum diffusion. From Fig. 15(b), it is observed that for a larger value of Prandtl number, the nanoparticle concentration near the surface becomes higher, but this effect becomes reverse after a certain distance from the surface boundary. For large Prandtl number the nanoparticles' dispersion rate becomes high and this effect dies out away from the surface. The temperature at a point near the boundary rises with the Schmidt number, while this trend becomes reverse after some distance from the surface, which can be observed in Fig. 16(a). Figure 16(b) shows the mass deposition of nanoparticles near the boundary for small Sc . When the relative value

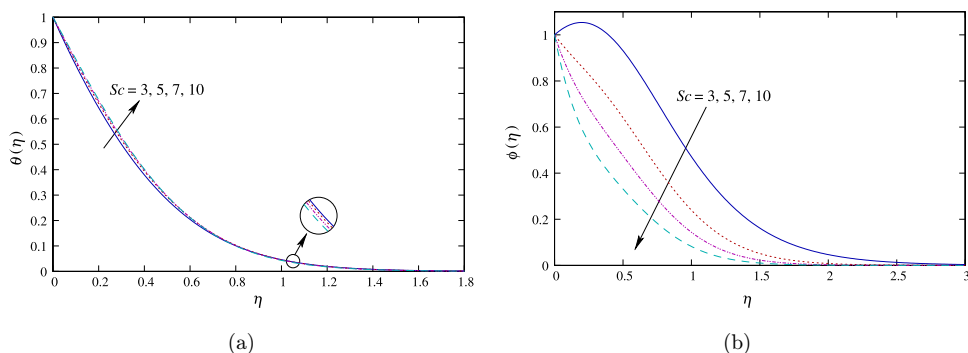


Fig. 16. (Color online) Effects of Schmidt number on the (a) temperature and (b) concentration with $A = 0.1$, $Nb = 0.1$, $Nt = 0.2$, $n = 0.5$, $m = 0.25$, $Pr = 6.8$, $\phi_1 = \phi_2 = 0.03$ and $\chi = 0.3$.

of momentum diffusion in comparison to mass diffusion rises, the nanoparticle concentration becomes less at every point in the fluid region and consequently, the concentration BLT becomes smaller.

5. Summary of Main Findings


This work is designed for examining the various aspects of the time-dependent flow of a hybrid nanofluid past a parabolic surface. The mathematical model for the problem is formulated through the revised Buongiorno model. Some important findings from this study are summarized as follows:

- A larger amount of Cu nanoparticles than alumina causes greater enhancement of surface drag along with cooling, whereas a larger amount of alumina yields almost the same cooling rate with less surface drag.
- To improve the cost efficiency along with higher cooling rate, a suitable combination of Cu and Al_2O_3 nanoparticle volumes needs to be selected.
- Maximum enhancements in the drag force and rate of transportation of heat can be seen for $\phi_1 = \phi_2 = 0.05$, which are 41.8% and 22.7% higher to those of water, respectively.
- Drag force in magnitude is low for thinner surfaces, while the heat and mass transfer rates show an enhancing trend for the thicker surfaces.
- Nanoparticles (Cu and Al_2O_3) addition significantly improves the heat and mass transfer rates, except in the case of mass transport rate for very slender surface with alumina addition.
- Unsteadiness intensifies surface cooling and drag force, while the reverse trend is followed for mass transport rate.
- The thermal and solutal BLTs decrease with power-law index and heat and mass transport rates' augmentations. But the opposite trends are followed for power-law exponent.
- Copper nanoparticles slow down the motion of hybrid nanofluid with 3% alumina, while alumina suspension increases the mobility of the hybrid nanofluid with 3% copper.
- All BLTs (momentum, thermal and concentration) reduce with the thickness of the parabolic surface.


Acknowledgments


The work of S. Rajput [09/013(0843)/2018-EMR-I] is supported by CSIR, India and K. Bhattacharyya acknowledges the "Faculty Incentive Grant" (No. R/Dev/D/IoE/Incentive/2022-23/47686) of Banaras Hindu University. Authors would also like to express their sincere thanks to the reviewers for their really fruitful suggestions.

ORCID

Sohita Rajput  <https://orcid.org/0000-0001-7102-303X>

Krishnendu Bhattacharyya  <https://orcid.org/0000-0001-7975-0709>

Dimpal Sharma  <https://orcid.org/0009-0005-3653-4076>

Ali J. Chamkha  <https://orcid.org/0000-0002-8335-3121>

References

1. R. Saidur, K. Y. Leong and H. A. Mohammed, *Renew. Sustain. Energy Rev.* **15**, 1646 (2011).
2. G. Huminic and A. Huminic, *Renew. Sustain. Energy Rev.* **16**, 5625 (2012).
3. E. Sadeghinezhad *et al.*, *Energy Convers. Manage.* **111**, 466 (2016).
4. K. Y. Leong *et al.*, *Renew. Sustain. Energy Rev.* **53**, 1092 (2016).
5. S. U. Choi, Enhancing thermal conductivity of fluids with nanoparticles, in *Developments and Applications of Non-Newtonian Flows*, eds. D. A. Singer and H. P. Wang, Vol. 66 (ASME, New York, 1995), pp. 99–105.
6. J. A. Eastman *et al.*, *Appl. Phys. Lett.* **78**, 718 (2001).
7. D. Wen and Y. Ding, *Int. J. Heat Mass Transf.* **47**, 5181 (2004).
8. A. Shafiq *et al.*, *Sci. Rep.* **11**, 13869 (2021).
9. A. Shafiq, T. N. Sindhu and Q. M. Al-Mdallal, *Sci. Rep.* **11**, 8812 (2021).
10. R. J. P. Gowda *et al.*, *Appl. Nanosci.* **13**, 585 (2023).
11. G. Rasool *et al.*, *Entropy* **22**, 18 (2020).
12. A. Shafiq *et al.*, *Eur. Phys. J. Plus* **136**, 407 (2021).
13. A. B. Çolak, A. Shafiq and T. N. Sindhu, *Chin. J. Phys.* **77**, 2435 (2022).
14. N. H. Hamad, A. Wakif and A. Alshehri, *Waves Random Complex Media* (2022), doi: 10.1080/17455030.2022.2100944.
15. G. Rasool *et al.*, *Waves Random Complex Media* (2022), doi: 10.1080/17455030.2022.2074571.
16. M. Alghamdi *et al.*, *Case Stud. Therm. Eng.* **28**, 101428 (2021).
17. N. A. Shah *et al.*, *Case Stud. Therm. Eng.* **35**, 102046 (2022).
18. M. U. Ashraf *et al.*, *Numer. Methods Partial Differ. Equ.* **38**, 666 (2022).
19. L. Ali *et al.*, *Chin. J. Phys.* **77**, 1625 (2022).
20. S. Rajput *et al.*, *Proc. Inst. Mech. Eng. E, J. Process Mech. Eng.* **236**, 1023 (2022).
21. S. Rajput *et al.*, *Waves Random Complex Media* (2022), doi: 10.1080/17455030.2022.2063986.
22. J. R. Babu, K. K. Kumar and S. S. Rao, *Renew. Sustain. Energy Rev.* **77**, 551 (2017).
23. S. Suresh *et al.*, *Exp. Therm. Fluid Sci.* **38**, 54 (2012).
24. S. S. U. Devi and S. A. Devi, *Can. J. Phys.* **94**, 490 (2016).
25. S. U. Devi and S. A. Devi, *Niger. Math. Soc.* **36**, 419 (2017).
26. J. K. Madhukesh *et al.*, *Proc. Inst. Mech. Eng. E, J. Process Mech. Eng.* (2021), doi: 10.1177/09544089211039305.
27. S. S. Ghadikolaei *et al.*, *J. Mol. Liq.* **268**, 813 (2018).
28. M. Usman *et al.*, *Int. J. Heat Mass Transf.* **126**, 1347 (2018).
29. B. Ali *et al.*, *Chin. J. Phys.* **70**, 125 (2021).
30. S. M. Hussain, R. Sharma and A. J. Chamkha, *Chin. J. Phys.* **75**, 120 (2022).
31. R. K. Tiwari and M. K. Das, *Int. J. Heat Mass Transf.* **50**, 2002 (2007).
32. J. Buongiorno, *J. Heat Transf.* **50**, 240 (2006).
33. L. Ali *et al.*, *Chin. J. Phys.* **77**, 1963 (2022).
34. L. Ali, B. Ali and M. B. Ghori, *Comput. Math. Appl.* **109**, 260 (2022).

35. C. Yang et al., *J. Heat Transf.* **135**, 054504 (2013).
36. M. Sheikholeslami et al., *Comput. Fluids* **94**, 147 (2014).
37. A. Malvandi and D. D. Ganji, *J. Appl. Fluid Mech.* **9**, 2277 (2016).
38. P. G. Siddheshwar and K. M. Lakshmi, *Phys. Fluids* **31**, 084102 (2019).
39. M. Zaydan et al., *Case Stud. Therm. Eng.* **22**, 100726 (2020).
40. W. Owhaib, M. Basavarajappa and W. Al-Kouz, *Sci. Rep.* **11**, 20669 (2021).
41. G. Rasool and A. Wakif, *J. Therm. Anal. Calorim.* **143**, 2379 (2021).
42. E. A. Algehyne et al., *Waves Random Complex Media* (2022), doi: 10.1080/17455030.2022.2074570.
43. A. Wakif et al., *Int. Commun. Heat Mass Transf.* **133**, 105937 (2022).
44. L. L. Lee, *Phys. Fluids* **10**, 820 (1967).
45. R. T. Davis and M. J. Werle, *AIAA J.* **10**, 1224 (1972).
46. O. D. Makinde and I. L. Animasaun, *Int. J. Therm. Sci.* **109**, 159 (2016).
47. O. D. Makinde and I. L. Animasaun, *J. Mol. Liq.* **221**, 733 (2016).
48. I. L. Animasaun, *Alex. Eng. J.* **55**, 2375 (2016).
49. I. L. Animasaun and N. Sandeep, *Powder Technol.* **301**, 858 (2016).
50. T. Fang, J. Zhang and Y. Zhong, *Appl. Math. Comput.* **218**, 7241 (2012).
51. M. Khan et al., *Results Phys.* **7**, 4050 (2017).
52. J. O. Olabode et al., *Partial Differ. Equ. Appl. Math.* **4**, 100078 (2021).
53. S. R. R. Reddy and P. B. A. Reddy, *Propuls. Power Res.* **11**, 129 (2022).
54. A. Shafiq, A. B. Çolak and T. N. Sindhu, *Int. J. Numer. Methods Fluids* **93**, 3384 (2021).
55. A. Shafiq, A. B. Çolak and T. N. Sindhu, *Arab. J. Sci. Eng.* **48**, 2807 (2023).
56. M. K. Nayak et al., *Arab. J. Sci. Eng.* **45**, 5331 (2020).
57. H. B. Keller and T. Cebeci, *AIAA J.* **10**, 1193 (1972).
58. N. M. Sarif, M. Z. Salleh and R. Nazar, *Procedia Eng.* **53**, 542 (2013).
59. W. Jamshed, E. K. Akgül and K. S. Nisar, *Phys. Scr.* **96**, 065201 (2021).
60. S. Rajput et al., *JCIS Open* **8**, 100064 (2022).
61. A. K. Pandey et al., *Propuls. Power Res.* **12**, 153 (2023).
62. A. K. Pandey et al., *Forces Mech.* **11**, 100179 (2023).
63. C. Y. Wang, *ZAMM — J. Appl. Math. Mech./Z. Angew. Math. Mech.* **69**, 418 (1989).
64. R. S. R. Gorla and I. Sidawi, *Appl. Sci. Res.* **52**, 247 (1994).
65. W. A. Khan and I. Pop, *Int. J. Heat Mass Transf.* **53**, 2477 (2010).